RSC Advances

PAPER

View Article Online
View Journal | View Issue

Cite this: *RSC Adv.*, 2026, **16**, 25569

Influence of solution chemical properties and porous medium surface coatings on the transport and retention behavior of polystyrene microplastics

Abliz Abdurahman, *[a] Xiaoli Ma[a] and Rui Gao[b]

The transport and retention behavior of microplastics (MPs) in saturated porous media is a hot issue in the fields of ecological security and public health in contemporary society. In this study, the transport and retention behaviors of polystyrene microplastics (PS-MPs) in saturated porous media were systematically investigated under various environmental conditions, including humic acid (HA) concentration, ionic strength (IS), mass fraction of iron oxyhydroxide coated quartz sand (ω), and pH in the presence of HA. A series of column experiments were conducted, and all breakthrough curves and retention profiles were successfully simulated using a two kinetic sites attachment-detachment model (TKSADM) that distinguishes between chemical adsorption (Site 1) and physical retention (Site 2). Results demonstrated that increasing HA concentration from 1 to 10 mg L^{-1} enhanced PS-MP transport, which was attributed to HA adsorption creating steric hindrance and enhancing electrostatic repulsion. In contrast, HA conditions, increasing IS from 0.1 to 100 mM progressively suppressed MP transport, with model parameters revealing a dramatic 30-fold increase in physical retention rate (k_{att2}) and a 2.8-fold increase in chemical adsorption capacity (S_{max1}/C_0), reflecting the dual role of IS in compressing the electrical double layer and inducing HA conformational collapse. Increasing the mass fraction of iron oxyhydroxide coated quartz sand (ω from 0.15 to 0.75) substantially inhibited PS-MP transferability, with both chemical adsorption rate (k_{att1}) and physical retention rate (k_{att2}) increasing by 57% and 83%, respectively, accompanied by a 79% increase in S_{max1}/C_0. This balanced enhancement reflects the dual role of iron oxyhydroxide coatings: increased surface roughness creating physical straining sites and ≡Fe–OH groups providing abundant reactive sites for specific adsorption. Increasing pH from 6.0 to 10.0 substantially enhanced MP mobility, with all retention – related parameters decreasing monotonically: k_{att1} decreased by 34%, k_{att2} decreased by 52%, and S_{max1}/C_0 exhibited the most dramatic decline (71%), revealing a "pH-switching effect" on physical retention sites – activated at low pH and deactivated at high pH due to enhanced electrostatic repulsion and HA conformational extension. This study provides quantitative mechanistic insights into MP fate in subsurface environments and underscores the need to consider coupled effects of multiple environmental factors when predicting MP transport behavior.

Received 20th October 2025
Accepted 5th May 2026

DOI: 10.1039/d5ra08025h

rsc.li/rsc-advances

1. Introduction

With the extensive use and improper disposal of plastic products, microplastics (MPs) have been widely distributed in terrestrial and aquatic environments around the world,[1,2] and have entered porous medium systems through various pathways such as surface runoff,[3,4] irrigation,[5,6] and atmospheric deposition.[7–9] MPs have characteristics such as persistence,[10,11] bioaccumulation,[12,13] and potential toxicity.[10,14] They can adsorb coexisting contaminants such as heavy metals,[15] organic pollutants (*e.g.*, PFOA),[16] and pathogenic microorganisms,[17,18] forming "composite pollution carriers" that further amplify their ecological hazards.[19]

The transport and retention behaviors of MPs in porous media directly determine their environmental dispersion range, fate, and potential ecological exposure risks.[20–23] These processes are not a simple physical filtration process, but rather the result of the coupled effect of multiple factors, including the inherent characteristics of MPs (such as particle size, shape, density, surface charge, and functional groups), the chemical properties of the solution (pH, ionic strength (IS), dissolved organic matter (DOM) content), and the properties of the medium (pore structure, mineral composition, and the presence of biofilms).[3,6] Among these, the surface charge of MPs and porous medium particles exerts a decisive influence on the transport behavior of MPs within porous media. This effect primarily operates by regulating electrostatic interactions

[a]*Chemistry Department, College of Pharmacy, Xinjiang Medical University, Urumqi, 830017, China. E-mail: abliz@xjmu.edu.cn; 1065158755@qq.com*
[b]*Institute for Advanced Study, Chengdu University, Chengdu, 610106, China. E-mail: gaorui@cdu.edu.cn*

between particles. When MPs carry the same charge as the surfaces of porous media (such as sand grains, clay minerals, *etc.*), the electrostatic repulsion between them reduces the possibility of MPs being captured by the medium, thereby enhancing their transport capacity.[24,25] On the contrary, when the surface charge of the medium is opposite to that of the MPs, a strong electrostatic attraction promotes the adhesion and retention of MPs, greatly restricting their transport within the pores.[26,27]

In recent years, preliminary progress has been made in studying the transport of MPs within porous media.[28,29] IS and DOM further modulate the influence of surface charge. High IS can compress the double layer on the surface of MPs, weakening electrostatic repulsion, leading to the aggregation and retention of MPs that are otherwise prone to transport due to charge repulsion.[27,30] For example, in an environment containing calcium ions (Ca^{2+}), divalent cations can act as a "bridge" to connect negatively charged MPs and negatively charged medium surfaces, significantly enhancing retention.[31] Meanwhile, after DOM molecules (such as humic acid HA) are adsorbed onto the surface of MPs, they may increase their negative charge or provide steric hindrance effect, thereby promoting the transport of MPs under certain conditions.[30,32] The pH of the solution regulates the zeta potential by affecting the protonation state of functional groups on the surface of particles, thereby affecting particle transport behavior.[33,34] Under low pH conditions, the surface of the medium may partially protonate, reducing its negative or even positive charge, which is beneficial for the transport of negatively charged MPs. Under high pH conditions, the degree of deprotonation on the surface of the medium increases, the surface negativity increases, and the electrostatic repulsion between the negatively charged MPs increases, improving their transport performances.[25]

Systematically elucidating the transport mechanisms of MPs under the coupled effects of multiple factors is a scientific prerequisite for accurately predicting their environmental behavior and conducting risk assessments.[35,36] Nevertheless, most studies examine only the independent effects of a single factor or a few factors (such as IS, pH, and HA), overlooking the potential synergistic or antagonistic effects that may exist between different factors – a core characteristic of real-world complex environments. In addition, regarding the influence of chemical modification on the surface of the medium, especially the microscopic mechanism of how variable charge coatings such as iron oxyhydroxide can form a ternary interaction with MPs and HAs, it remains unclear. More importantly, most existing MPs transport studies employ single kinetic site models or equilibrium approaches,[37] which assumed that there is a specific type of active site in the reaction system, and all these sites are energetically homogeneous, with the same adsorption energy and reaction activation energy. Therefore, the structures and fitting processes of these models are relatively simple. However, they have the following fundamental limitations in describing the transport behavior of particulate matter, especially when conducting systematic parameter analysis for multiple environmental factors. (1) It is impossible to distinguish between these two fundamentally different processes: physical retention and chemical adsorption; (2) unable to fit the hyper-exponential decay retention profiles observed in experiments; (3) the differential effects of environmental factors on different sites cannot be explained; (4) they lack comparability with the widely applied two kinetic sites model studies in the field. These makes them difficult to accurately describe the potential differences in kinetic processes of MPs on heterogeneous surfaces. This gap hinders mechanistic understanding of how different environmental factors regulate MPs fate through distinct pathways.

To address the aforementioned research gap, this study systematically investigates the influence of key environmental factors – including HA concentration, IS, pH, and surface charge heterogeneity of quartz sand particles, on the transport and retention behavior of polystyrene model microplastics (PS-MPs) within saturated porous media systems. The research process employs two kinetic sites model to quantitatively analyze and deeply elucidate the relevant interaction processes and mechanisms, revealing the core control mechanisms under multi-factor coupling effects. This contributes to refining the theoretical framework for MPs environmental behavior within groundwater and soil porous media systems. It also provides crucial theoretical foundations and data support for scientifically assessing groundwater pollution risks from MPs and formulating targeted prevention, control, and remediation strategies for MPs contamination in soil and groundwater.

2. Materials and methods

2.1. Preparation of PS-MPs suspension

PS-MPs purchased from Sigma-Aldrich, Inc., USA. To prepare the PS-MPs stock solutions, 100 mg of the original PS-MPs powder was mixed into 1 L of deionized (DI) water and dispersed by an ultrasonic cleaner (KQ – 300VDE, Supmile, China) for 30 min to ensure complete dispersion of the particles. Prior to each column test, the PS-MPs stock solutions were diluted with the desired background solutions (HA, NaCl or both) to a target concentration 40 mg L^{-1}. The pH of each suspension of PS-MPs and their respective background solutions was set between 6.0 and 10.0 (6.0, 8.0 and 10.0) using solutions of 1.0 mM HCl or NaOH to achieve the desired adjustment. The concentration of PS-MPs suspension was determined using total organic carbon analyzer (TOC – L CPH, SHIMADZU, Japan). And the zeta potentials of PS-MPs in solutions varying in HA concentration, IS, and pH were measured using zeta potential analyzer (Zhongcheng Digital Technology model JS94G, China) (see SI).

2.2. Porous media

Quartz sand (Shaanxi Zhouzhi County Quartz Sand Co, Ltd China) was selected for the column tests as the porous medium, with a particle size range of 10–20 mesh. Before the experiment, the quartz sand was treated in 10% (V : V) HNO_3 solution for 24 h to remove the impurity, and then cleaned with tap water and DI water until the pH of the aqueous solution reached

a neutral level.[28] Then dry overnight at 105 °C and store in a sealed container for later use.

Quartz sand coated with iron oxyhydroxides are prepared according to the method reported by Stahl *et al.*[38,39] 500 g of quartz sand was added to an evaporating dish and then 0.17 mol L^{-1} of Fe $(NO_3)_3$ 387.5 mL and 0.52 mol L^{-1} of NaOH 90 mL were held to precipitate onto the quartz sand. The mixture was placed in a drying oven at 105 °C for 72 hours with periodic stirring to prevent salt crusting on the surface of the quartz sand. The quartz sand was washed with 1.0 mM HCl and 1.0 mM NaOH to remove the poorly adsorbed iron on the surface of the quartz sand. Scanning electron microscopy–energy dispersive X-ray analysis (SEM–EDX) (SSX – 550, Shimadzu, Japan) results showed that 75 ± 3% of the quartz sand surface were coated with iron oxyhydroxides.[38,40] Finally, the zeta potentials of bare and iron oxyhydroxides coated quartz sand were measured by zeta potential meter (BI – EKA, Brookhaven Instruments Corp., Holtsville, NY) under the same conditions as in the subsequent column experiments (see SI).

2.3. Column experiments

PS-MPs transport experiments were conducted using glass chromatography columns (with diameter of 2.6 cm and a length of 12 cm) packed with wet quartz sand (Fig. 1). The porosity of the sand columns determined gravimetrically according to the method outlined by Jaisi *et al.*[41] and it varied between 0.37 to 0.40. In the experiment on the effect of iron oxyhydroxide surface coatings on the transport and retention of PS-MPs, the porous medium was prepared by uniformly mixing surface coated quartz sand and bare quartz sand in different mass ratios.[38]

The column experiments were completed with the assistance of a peristaltic pump (BT100L, Baoding Fluid Technology Co., Ltd, China) in the down-flow mode at a flow rate of 1 mL min^{-1} (Darcy velocity of 3.13 × 10^{-6} cm s^{-1}) to maintain the stability of the experimental conditions, and various conditions as detailed in Table 1. Initially, the quartz sand column was rinsed with DI water until no visible impurities were present in the effluent. Subsequently, the chosen background solution was infused into the column for 3 h to create stable chemical conditions. Then, PS-MPs suspension in 4 PV of the same background solution was passed through the column. Finally, several PVs background solutions introduced to the column to flush out the unattached PS-MPs. During the experiment, the effluent was manually collected every 4 minutes, and the concentration of PS-MPs determined by the total organic carbon analyzer (TOC – L CPH, Tsushima, Japan). Following the completion of each transport test, each column was dissected into 12 layers of 1 cm segments, and the quartz sand grains in each fraction were extracted with DI water to determine spatial distribution profile of retained PS-MPs, as described earlier studies.[38,40] All column tests were performed at least twice.

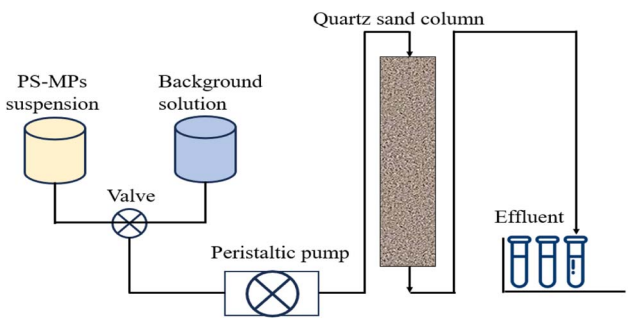

Fig. 1 Column experimental apparatus.

The PS-MPs breakthrough curves (BTCs) was plotted as a function of the pore volume (PV) as the horizontal coordinate and the standardized concentration of PS-MPs in the effluent, C/C_0 (dimensionless), as the vertical coordinate. The retention profiles (RPs) were plotted based on the functional relationship between the standardized concentration S/C_0 [M^{-1}] of PS-MPs in each gram of quartz sand and the column depth, to explore the retention distribution of PS-MPs in the sand column. Finally, the sum of the masses of PS-MPs in the effluent and retained in the quartz sand column will be compared with the mass of the PS-MPs injected into the column to calculate the mass balance. In addition, the tracer experiment was conducted under similar experimental conditions using a tracer solution (0.2 mM KNO_3, with NO^{3-} as the tracer), and the concentrations of NO^{3-} were quantified by UV-Vis Spectrophotometer at 220 nm.[37]

2.4. Mathematical model

Derjaguin–Landau–Verwey–Overbeek (DLVO) theory was used to evaluate the interaction energy between PS-MPs and quartz sand across various experimental scenarios. The total interaction energy (Φ_{total}) between particles is the sum of van der Waals forces (Φ_{vdw}) and electrostatic interactions (Φ_{elec}).[42] The PS-MPs–quartz sand system is considered as a ball–plate interaction system[43] to estimate the interaction energy (see SI).

The tracer transport was described by the one-dimensional (1D) advection and dispersion model (ADE):

$$\frac{\partial C}{\partial t} = -v\frac{\partial C}{\partial x} + D_L\frac{\partial^2 C}{\partial^2 x}$$

where C [M L^{-3}] is the tracer (KNO_3) concentration in the liquid phase, t [T] is time, v [L T^{-1}] is the pore water velocity, x [L] is the flow length, which is 12 cm in this work, and D_L [L^2 T^{-1}] is the longitudinal dispersion coefficient.

The transport of MPs in porous media is a highly complex process involving transport, attachment, detachment, blocking, straining, release, aggregation, and sedimentation.[26,32,44,45] Therefore, its transport and retention are governed by a combination of various mechanisms.[46,47] In this study, the transport of PS-MPs are described by coupling the advection–dispersion equation with a two kinetic sites attachment-detachment mode (TKSADM).[48,49] Mathematical expression of this model is as follows:[28,48–51]

$$\frac{\partial(\theta C)}{\partial t} + \rho_b\frac{\partial(S_1)}{\partial t} + \rho_b\frac{\partial(S_2)}{\partial t} = \frac{\partial}{\partial x}\left(\theta D\frac{\partial C}{\partial x}\right) - \frac{\partial qC}{\partial x}$$

where, C [M L^{-3}] is the PS-MP concentration in the liquid phase, t [T] is the time, and θ [L^3 L^{-3}] is the volumetric water content, ρ_b [M L^{-3}] is the bulk density of the quartz sand, D [L^2 T^{-1}] is the hydrodynamic dispersion coefficient, q [L T^{-1}] is the Darcy flux.

Table 1 Zeta potentials of PS-MPs and quartz sand, and the calculated interaction energy between PS-MPs and quartz sand based on the classical DLVO theory

				Zeta potentials (mV)		Φ^f
HA[a] (mg L^{-1})	IS[b] (mM)	ω^c	pH	PS-MPs[d]	Quartz sand[e]	($\times 10^4$ kT)
0	0.1	0	6.0	−57.36 ± 0.54	−26.38 ± 0.63	346
1	0.1	0	6.0	−59.45 ± 0.69	−29.15 ± 1.35	418
5	0.1	0	6.0	−61.79 ± 0.31	−29.87 ± 0.36	455
10	0.1	0	6.0	−61.84 ± 1.40	−30.85 ± 1.62	492
10	1	0	6.0	−61.43 ± 1.00	−28.82 ± 0.57	28.5
10	10	0	6.0	−50.82 ± 3.45	−28.06 ± 2.01	11.1
10	100	0	6.0	−31.09 ± 2.75	−22.64 ± 1.14	0.624
10	0.1	0.15	6.0	−61.84 ± 1.40	−24.43 ± 0.24	34.8
10	0.1	0.30	6.0	−61.84 ± 1.40	−17.96 ± 0.31	21.2
10	0.1	0.45	6.0	−61.84 ± 1.40	−11.63 ± 0.08	9.42
10	0.1	0.60	6.0	−61.84 ± 1.40	−5.590 ± 0.38	0.496
10	0.1	0.75	6.0	−61.84 ± 1.40	1.410 ± 0.11	—[g]
10	0.1	0.15	8.0	−65.03 ± 1.13	−29.82 ± 0.25	46.8
10	0.1	0.15	10.0	−66.21 ± 5.52	−33.61 ± 0.41	58.6

[a] Humic acid (pH 6.0). [b] Ionic strength (NaCl as background electrolyte). [c] Fraction of the quartz sand grain surfaces coated by iron oxyhydroxide. [d] Zeta potential of PS-MPs. [e] Zeta potential of quartz sand or average value of uncoated/coated quartz sand grain. [f] Energy barriers between PS-MPs and quartz sand calculated by DLVO theory. [g] Electrostatic attraction predominates between polystyrene PS-MPs and quartz sand particles, and there is no energy barrier that hinders particle contact.

In the equation, the first term on the left-hand side represents the rate of change of the liquid-phase concentration of PS-MPs over time. The second and third items on the – hand side represents the rates of change in PS-MPs retention in the solid phase at site 1 (S_1) and site 2 (S_2) over time. The first item on the right-hand side is the diffusion term, which describes the diffusion driven by the concentration gradient of PS-MPs. The second item is the convection term, which describes the transport of PS-MPs carried by water flow.

In this study, two types of kinetic sites S_1 and S_2 are representing chemical adsorption sites and physical straining sites, respectively.[50,51] Among them, S_1 typically corresponds to an adsorption process dominated by surface chemical forces (DLVO forces).[50,51] PS-MPs attach to the surface of sand grains through electrostatic attraction, van der Waals forces, *etc.* The capacity of such sites is limited;[50,51] as deposited PS-MPs occupied the surface of porous medium particles, subsequent adsorption is inhibited. And S_2 typically corresponds to a physical retention mechanism. It is a purely geometric mechanism by which PS-MPs are trapped in a porous medium. When a PS-MPs size is greater than or close to the size of a pore throat, the particles cannot pass through and is physically retained. A key characteristic of this process is significant spatial heterogeneity: near the injection end (the column inlet), the pore throats become blocked first, and the straining efficiency decreases more rapidly the deeper one goes into the medium.[50,51] The kinetic equations for each of the two sites are:[38,40,50,51]

$$\rho_b \frac{\partial(S_1)}{\partial t} = \theta k_{att1} \psi_1 C - \rho_b k_{det1} S_1$$

$$\rho_b \frac{\partial(S_2)}{\partial t} = \theta k_{att2} \psi_2 C - \rho_b k_{det2} S_2$$

where k_{att1} [T^{-1}] and k_{att2} [T^{-1}] are the first-order rate constants for the attachment of PS-MPs to S_1 and S_2, k_{det1} [T^{-1}] and k_{det2} [T^{-1}] are the first-order rate constant for the detachment of PS-MPs from S_1 and S_2 back into the aqueous phase. ψ_1 and ψ_2 are respectively representing the retention functions of S_1 and S_2. The classic Langmuir blocking function is the retention function for the S_1, which is mainly controlled by solution chemistry and surface chemistry. Its mathematical expression is:[51–53]

$$\psi_{att1} = 1 - \frac{S_1}{S_{max1}}$$

where S_1 is the current solid-phase retention concentration of PS-MPs at site 1, S_{max1} is the maximum retention capacity, which represents the maximum solid-phase concentration of PS-MPs that can attach to S_1. As for S_2, the depth-dependent straining function is adopted:[50,51]

$$\psi_{att2} = \left(\frac{d_{50} + x - x_0}{d_{50}}\right)^{-\beta}$$

where d_{50} [L] is the median particle size, x_0 [L] is the reference distance (typically taken as the coordinates at the column inlet), x [L] is the distance of PS-MPs from the column inlet, and β [–] is the empirical factor that controls the shape of the PS-MPs RPs, which is set as 0.432.[49]

The transport and retention parameters (D, k_{att1}, k_{att2}, k_{det1},k_{det2} S_{max1}) of the BTCs and RPs obtained from the column experiments of the tracer (NO^{3-}) and PS-MPs were fitted using the hydrodynamic software HYDRAUS-1D[54] and optimized by least square method.[55]

In studies of MPs transport within saturated porous media, attachment efficiency (α) serves as a core parameter for quantifying the probability of actual attachment occurring after MPs collide with porous media surfaces. It directly links theoretical

collision frequency to actual retention behavior, making it crucial for predicting the environmental fate of MPs.[22] In the Physicochemical Filtration Theory (PCPT), the attachment efficiency α is central to evaluating the trapping mechanism of particles within porous media, particularly their transport behavior in water-saturated porous media.[42] In our research, we assumed that α is not a single fitting parameter but is instead "allocated" across two attachment pathways:

$$\alpha_{\text{total}} \approx \alpha_{S_1} + \alpha_{S_2}$$

The two terms on the right-hand side of equation correspond to the "effective" attachment efficiencies at S_1 and S_2, respectively, and can be explicitly expressed in terms of rate constants:[56]

$$\alpha_{S_1} = \left(\frac{2}{3}\right) \times \left(\frac{d_c}{1-\theta}\right) \times \left(\frac{1}{q}\right) \times \frac{1}{\eta_0} \times k_{\text{att1}}$$

$$\alpha_{S_2} = \left(\frac{2}{3}\right) \times \left(\frac{d_c}{1-\theta}\right) \times \left(\frac{1}{q}\right) \times \frac{1}{\eta_0} \times k_{\text{att2}}$$

where η_0 [–] is the single-collector contact efficiency of quartz sand, and it is determined by three physical capture mechanisms: Brownian diffusion η_D, direct interception η_I, and gravitational sedimentation η_G.[57] Its specific mathematical expression is (see SI 5):

$$\eta_0 = \eta_D + \eta_I + \eta_G$$

Ultimately, the value of α can be calculated with column transport experimental data based on the following expression:

$$\alpha_{\text{total}} = \left(\frac{2}{3}\right) \times \left(\frac{d_c}{1-\theta}\right) \times \left(\frac{1}{q}\right) \times \frac{1}{\eta_0}(k_{\text{att1}} + k_{\text{att2}})$$

3. Result and discussion

3.1. Characterization of PS-MPs and quartz sand

According to the scanning electron microscope (SEM) (SU8010, Hitachi, Japan) test results, the PS-MPs are spherical in shape (Fig. 2A). Based on Dynamic Light Scattering (DLS) analysis (MasterSizer 2000, Malvern Instruments, UK), the size of PS-MPs in ultrapure water (18.2 MΩ cm, prepared by the Milli-Q system) at pH 6.0 ranged from 3.31 to 138 μm, and the median diameter (D_{50}) is about 10.6 ± 0.2 μm (Fig. 2B), this is exactly the same as the average particle size of 10 μm provided by the supplier. The specific surface area (SSA) of PS-MPs is 0.98 ± 0.32 $m^2\ g^{-1}$ determined by Brunauer–Emmett–Teller (BET) method (ASAP 2460, Micromeritics, US).

The particle size test results show that the average particle size of bare quartz sand is approximately 1.76 ± 0.35 mm (n = 1000). The surface morphology and elemental composition of quartz sand was measured by scanning electron microscope (SU8010, Hitachi, Japan) combined with energy dispersive X-ray spectrometer (EDS), and the results are shown in Fig. 3. As shown in Fig. 3A, quartz sand particles exhibit an irregular blocky morphology with well-defined individual particle outlines. The particle surfaces are rough, featuring naturally fractured textures with uneven patterns and irregular edges. No obvious signs of artificial modification or chemically eroded surface features were observed, reflecting their primary clastic morphology. The EDS spectrum (Fig. 3B) exhibits strong characteristic peaks for Si (energy ≈ 1.7 keV) and O (energy ≈ 0.5 keV), which are the dominant elemental signals in the sample. Their relative signal intensities align with the elemental composition ratio of SiO_2, the primary component of quartz sand. Additionally, the weak C peak (≈0.2 keV) in the spectrum originates from environmental carbon-based contaminants adsorbed on the sample surface. The Pt peak (≈2.0 keV) corresponds to the conductive platinum layer sprayed onto the sample surface prior to SEM testing (to enhance the conductivity of insulating quartz sand for testing). While the Fe peak (≈6.4 keV) represents a characteristic peak for trace impurities, indicating the presence of minimal iron–based impurity components in the sample.

3.2. Effect of HA concentration on transport and retention of PS-MPs

To explore the effect of DOM in pore solution on the transport of MPs in porous media, HA is employed to conduct the column experiments, and the BTCs and RPs of PS-MPs under different HA concentrations are shown in Fig. 4. The results revealed that the presence of HA clearly facilitated the transport of PS-MPs under all examined conditions. As the HA concentration increased, the transportability of PS-MPs was enhanced, and the promoting effect of HA exhibited strong dependence on HA concentration. For example, when HA concentration increased

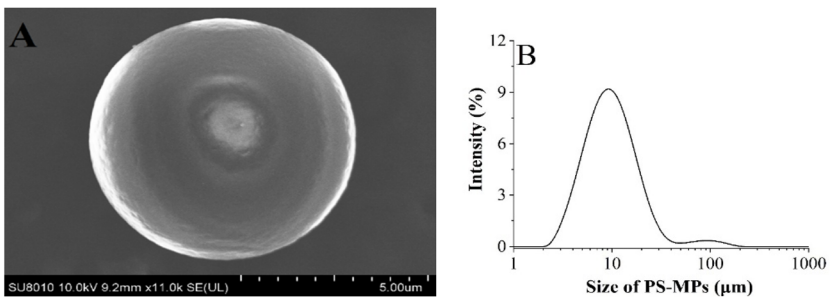

Fig. 2 SEM image (A) and hydrodynamic diameter distribution (B) of PS-MPs.

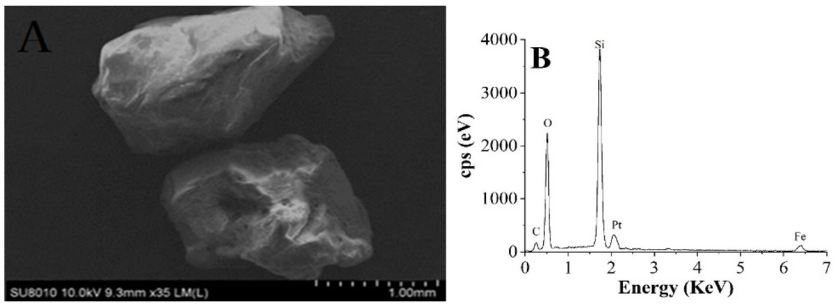

Fig. 3 SEM image (A) and EDS spectrum (B) of uncoated quartz sands.

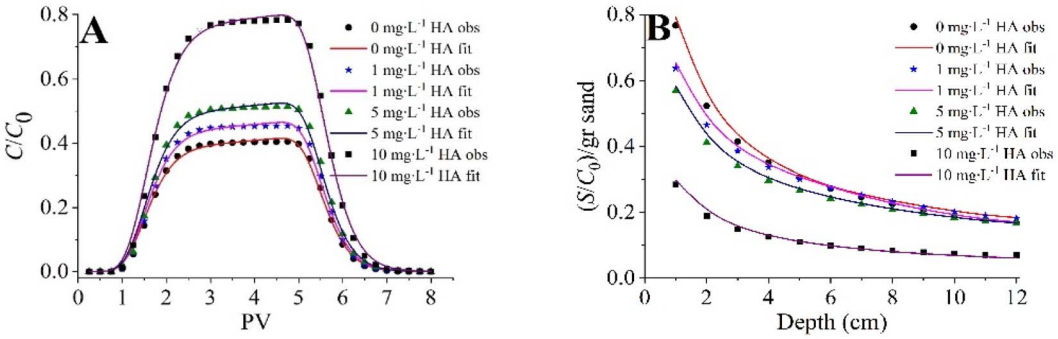

Fig. 4 Measured and fitted breakthrough curves (A) and retention profiles (B) for PS-MPs at different HA concentration at pH 6.0 in uncoated quartz sand.

from 0 to 10 mg L^{-1}, the C/C_0 of PS-MPs rose from 0.442 to 0.799, and the calculated α values of PS-MPs decreased from 0.052 to 0.014 (Table 2). Correspondingly, the effluent rates increased from 49.80% to 84.51%, and the retention rates of PS-MPs were decreased from 48.90% to 17.82% (Table 2). Additionally, under HA conditions, the PS-MPs recovery rates are relatively high (97.01 to 102.33%) and almost all of them are recovered. Similar promotion effects of HA have been observed on the transport of other MPs and engineering inorganic nanoparticles (EINs).[31,58]

The facilitated transport of PS-MPs attributed to HA involves electrostatic interaction, steric repulsion, and competition for available adsorption sites on quartz sand surfaces. Initially, as listed in Table 1, all the studied PS-MPs and quartz sand grains carry more negative charges with presence of HA in the solution. And, as the HA concentration increased, the absolute value of

Table 2 Mass balance percentages for PS-MPs in saturated packed column experiments at varying HA concentration, IS, iron oxyhydroxides coating, and pH

HA mg L^{-1}	IS mM	ω	pH	$(C/C_0)_{max}$	α	M_{eff}[a]%	M_{ret}[b]%	$M_{ret\text{-}inlet}$[c]%	M_{tot}[d]%
0	0.1	0	6.0	0.442	0.052	49.80	48.90	24.50	98.70
1	0.1	0	6.0	0.466	0.049	52.67	46.72	23.40	99.39
5	0.1	0	6.0	0.526	0.041	54.40	41.64	20.67	97.01
10	0.1	0	6.0	0.799	0.014	84.51	17.82	9.78	102.3
10	1	0	6.0	0.743	0.019	84.14	22.55	12.44	106.7
10	10	0	6.0	0.483	0.046	50.81	45.57	22.39	96.38
10	100	0	6.0	0.369	0.063	38.70	54.54	28.07	93.24
10	0.1	0.15	6.0	0.615	0.031	65.36	35.04	15.57	100.4
10	0.1	0.30	6.0	0.528	0.041	55.83	41.68	20.14	97.51
10	0.1	0.45	6.0	0.464	0.049	48.88	46.83	23.30	95.71
10	0.1	0.60	6.0	0.441	0.052	44.42	51.31	24.80	95.73
10	0.1	0.75	6.0	0.391	0.060	40.99	52.49	27.17	93.49
10	0.1	0.15	8.0	0.725	0.020	76.37	26.01	11.68	102.4
10	0.1	0.15	10.0	0.756	0.018	79.57	23.36	10.61	102.9

[a] Refers to the effluent percentage of PS-MPs recovered from column tests. [b] Refers to the retained percentage of PS-MPs recovered from column tests. [c] Refers to the PS-MPs retained near the column inlet. [d] Refers to the total percentage of PS-MPs recovered from column tests.

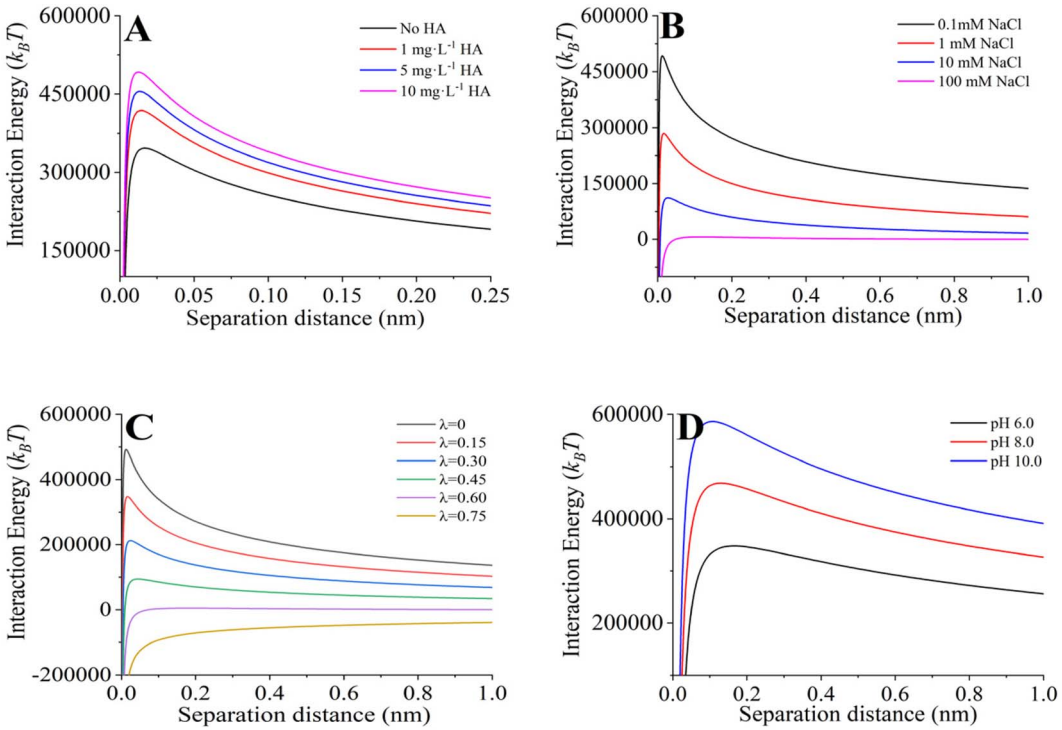

Fig. 5 DLVO energy profiles of PS-MPs and quartz sand surface under different experimental conditions. (A) The influence of HA concentration at pH 6.0. (B) The influence of IS at pH 6.0 with 10 mg L^{-1} HA. (C) The influence of surface charge heterogeneity of quartz sand in 0.1 mM NaCl with 10 mg L^{-1} HA. (D) The influence of pH in 0.1 mM NaCl with 10 mg L^{-1} HA.

their zeta potential increased. This is mainly because HA regulates the negative charge density on the particle surface through surface adsorption.[59–61] Thus, electrostatic repulsion between PS-MPs and quartz sand grains is improved. The relatively higher DLVO energy barriers (Φ_{max}) between PS-MPs and quartz sand grains are observed (Fig. 5) with the presence of HA in solution, causing PS-MPs to be difficult to capture by quartz sand particles, leading to enhanced transport of PS-MPs in sandy column. Then, at higher concentrations (such as 10 mg L^{-1}), Steric hindrance caused by HA prevented PS-MPs from agglomerating,[42,62] as confirmed by inverted microscope images (Fig. 5), and further enhanced the transport of PS-MPs in sandy column. Previous studies have also reported that the improvement in particle transport performance under HA conditions is attributed to changes in particle surface charge due to HA adsorption and the decomposition of previously aggregated particles.[37,60,63,64] Lastly, HA may compete with PS-MPs for adsorption on quartz sand surfaces,[60,65] reducing the number of active adsorption sites available for PS-MPs. This could also weaken the retention of PS-MPs within the column.

RPs of PS-MPs under different concentrations of HA conditions are presented in Fig. 4B. Under all tested conditions, the RPs exhibited a hyper-exponential decay pattern, characterized by substantial retention near the column inlet (0–4 cm) followed by a sharp decline and relatively low retention in deeper sections, and the hyper-exponential RPs were more pronounced at low HA concentrations. For instance, at 1 mg L^{-1} HA, approximately 50.08% of the total retained PS-MPs were found in the first 4 cm of the column, while only 49.91% was retained beyond 8 cm (Table 2). This is similar to the results of some previous studies.[38]

The observed hyper-exponential retention profiles can be attributed to the combined effects of physical straining, pore throat trapping and chemical heterogeneity.[66] The greater retention near the column inlet compared to the outlet is not simply due to $k_{att1} > k_{att2}$, but rather reflects the spatial distribution of S_2 retention mechanisms.[44,45,67] Physical straining and pore throat trapping occur preferentially near the inlet because: (i) the probability of encountering pore constrictions is highest at the column entrance, and (ii) once particles are captured, they are removed from the mobile phase and cannot travel further. This spatial bias, combined with the high k_{att1} values, produces the characteristic hyper-exponential retention profiles. In contrast, chemical adsorption (S_2) can occur throughout the column wherever reactive surface sites are accessible, contributing to the low but non-zero retention observed in deeper sections.[68]

3.3. Effect of IS on transport and retention of PS-MPs

Under HA conditions, the effects of IS on the transport and retention behaviors of PS-MPs in bare sandy column were illustrated in Fig. 6. The transportability of PS-MPs in the saturated sandy column decreased as the IS increased. Specifically, as shown in the Fig. 7A, the transport velocities of PS-MPs decreased with increased IS, resulting in delayed and broadened BTCs. As lowest IS (0.1 mM) presence in HA solution, C/C_0

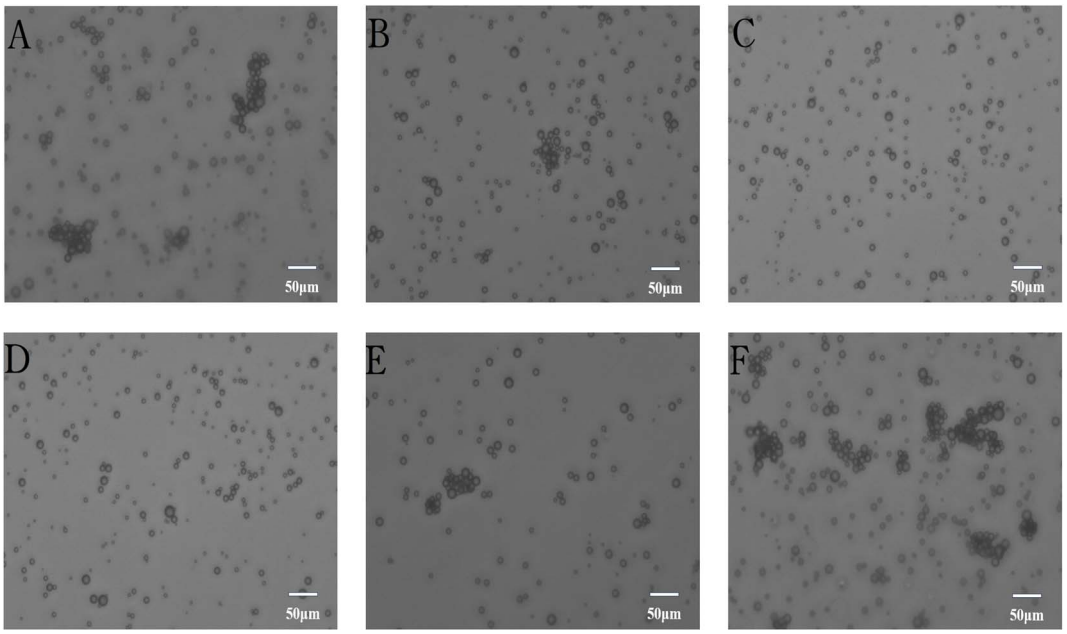

Fig. 6 Inverted micrographs of PS-MPs in different background solutions. (A) 0.1 mM of NaCl solution with no HA. (B) 1 mg L^{-1} HA solution with 0.1 mM of NaCl. (C) 10 mg L^{-1} HA solution with 0.1 mM of NaCl. (D) 10 mg L^{-1} HA solution with 1.0 mM of NaCl. (E) 10 mg L^{-1} HA solution with 10 mM of NaCl. (F) 10 mg L^{-1} HA solution with 100 mM of NaCl, pH of all solutions adjusted to 6.0.

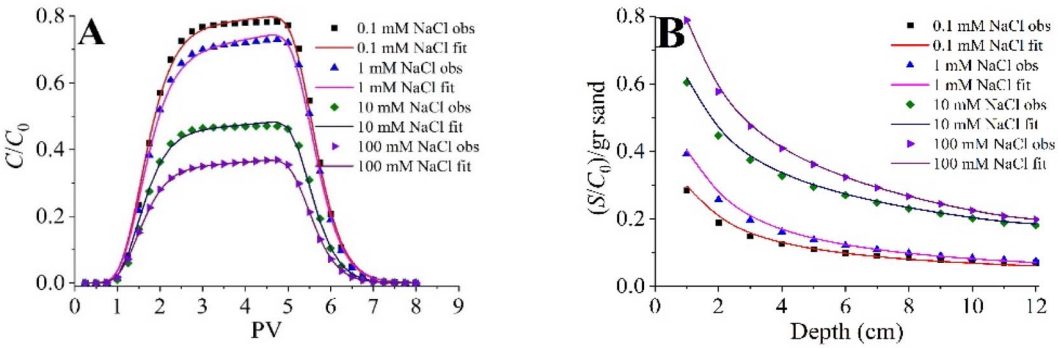

Fig. 7 Measured and fitted breakthrough curve (A) and retention profiles (B) for PS-MPs under different IS at pH 6.0 in the presence of 10 mg L^{-1} HA.

and outflow rates of PS-MPs were as high as 0.799 and 84.51%, respectively, while they decreased to 0.369 and 38.70% in solution with 100 mM (Table 2). An increase in the α values of PS-MPs are observed as the solution IS increased, especially at high solution IS (Table 2). This indicated that increased IS not only slows transport rates but also reduces the transport capacity of PS-MPs. This is consistent with the transport trend of other nanoparticles (such as nHAP) under different IS with HA conditions.[38]

Under the tested IS conditions, the zeta potentials of PS-MPs, and quartz sand were negative (Table 1). And the zeta potentials of them became less negative as the IS increased, mainly due to the compressed double layer and the shielding charge effect of Na^+.[69] For example, when IS increased from 0.01 mM to 100 mM, the zeta potential of PS-MPs and quartz sand changed from −61.84 mV and −30.85 mV to −31.09 mV and −22.64 mV, separately. Therefore, the increase in IS resulted in reduced electrostatic repulsion forces between PS-MPs with quartz sand (Fig. 4), leading to increased deposition in the sandy columns.[64,70–72] Additionally, the weakening of electrostatic repulsion between PS-MPs leads to their self-agglomeration, resulting in an increase in particle size[64,73] (Fig. 6). These large particles are prone to physical trapping in the pore structure of quartz sand.[45,74] However, HA enhanced the transport ability of MPs through steric hindrance and electrostatic repulsion,[63,75] but this effects weakened by the ion shielding effect under high IS conditions.[76,77] High concentrations of ions compress the molecular structure of HA, reducing its steric hindrance ability, while also promoting the co-agglomeration of HA and PS-MPs, further exacerbating particle deposition.[78,79]

Under the presence of HA, the RPs of PS-MPs in all IS treatment groups exhibited hyper-exponential decay characteristics,

Table 3 Fitted parameters of the two kinetic sites attachment-detachment model as estimated from the breakthrough data for saturated packed column at varying HA concentration, IS, iron oxyhydroxides coatings, and pH

HA (mg L^{-1})	IS (mM)	ω	pH	k_{att1}[a] (min^{-1})	k_{det1}[b] (min^{-1})	k_{att2}[c] (min^{-1})	k_{det2}[d] (min^{-1})	S_{max1}/C_0[e] (S/C_0) (g^{-1})	R^{2f}
0	0.1	0	6.0	4.98×10^{-1}	1.08×10^{-5}	7.99×10^{-2}	1.54×10^{-8}	2.09	0.999
1	0.1	0	6.0	4.88×10^{-1}	1.66×10^{-6}	7.18×10^{-2}	5.07×10^{-8}	2.05	0.997
5	0.1	0	6.0	4.62×10^{-1}	9.25×10^{-7}	5.50×10^{-2}	6.27×10^{-8}	1.68	0.995
10	0.1	0	6.0	3.61×10^{-1}	5.32×10^{-7}	3.28×10^{-3}	6.51×10^{-8}	0.74	0.998
10	1	0	6.0	4.59×10^{-1}	8.10×10^{-7}	5.61×10^{-3}	6.46×10^{-8}	0.98	0.997
10	10	0	6.0	4.93×10^{-1}	8.16×10^{-7}	7.11×10^{-2}	1.93×10^{-8}	1.92	0.997
10	100	0	6.0	5.46×10^{-1}	1.01×10^{-6}	1.02×10^{-1}	1.36×10^{-8}	2.78	1
10	0.1	0.15	6.0	3.72×10^{-1}	1.90×10^{-6}	5.45×10^{-2}	9.08×10^{-9}	1.42	1
10	0.1	0.30	6.0	3.88×10^{-1}	1.95×10^{-6}	6.10×10^{-2}	8.54×10^{-9}	1.83	1
10	0.1	0.45	6.0	4.65×10^{-1}	6.40×10^{-6}	7.36×10^{-2}	7.78×10^{-9}	2.25	1
10	0.1	0.60	6.0	5.59×10^{-1}	9.36×10^{-6}	9.94×10^{-2}	7.40×10^{-9}	2.50	1
10	0.1	0.75	6.0	5.85×10^{-1}	1.07×10^{-5}	9.98×10^{-2}	6.66×10^{-9}	2.54	0.999
10	0.1	0.15	8.0	2.44×10^{-1}	1.01×10^{-6}	3.33×10^{-2}	9.46×10^{-8}	0.50	0.999
10	0.1	0.15	10.0	2.40×10^{-1}	8.14×10^{-7}	2.61×10^{-2}	9.56×10^{-8}	0.41	0.994

[a] First-order retention coefficient on S_1. [b] First-order detachment coefficient on S_1. [c] First-order retention coefficient on S_2. [d] First-order detachment coefficient on S_2. [e] Maximum solid phase concentration of PS-MPs on S_1 normalized by the input PS-MPs concentration. [f] Squared Person's correlation coefficient.

meaning that the retention concentration decreased rapidly and non-linearly with distance. Retention levels at the inlet end (0–4 cm) were significantly higher than in the latter half of the column (Fig. 6B). Notably, the hyper-exponential decay characteristic intensified with increased IS. Under low IS conditions (0.1 mM NaCl), the retention curve is relatively flat, with retention levels as high as 9.78% at the inlet end (0–4 cm). When the IS increased to 100 mM, the hyper-exponential decay characteristic was most pronounced, with retention levels as high as 28.07% at the inlet end (0–4 cm) (Table 2).

Under HA conditions, TKSAD model provided excellent fits for experimental data across all IS treatment groups ($R^2 > 0.997$, Table 3). Model parameters revealed a significant regulatory effect of IS on the retention mechanism of PS-MPs. As the IS increased from 0.1 mM to 100 mM, the attachment rate k_{att1} at S_1 monotonically increased from 0.361 min^{-1} to 0.546 min^{-1}, representing an approximate 51% increase. Concurrently, the maximum retention capacity S_{max1}/C_0 at S_1 substantially increased from 0.74 to 2.78 g^{-1}, representing a 2.8-fold increase (Table 3). This indicates that high IS not only accelerates the kinetic rate of chemical adsorption, more importantly, creates additional physical retention sites. This may be attributed to MPs agglomeration caused by HA conformation collapse and the formation of uneven organic coatings on the surface of the medium by HA. Notably, the adsorption rate constant k_{att2} at S_2 exhibits a more pronounced response to IS: it increases sharply from 0.00328 min^{-1} at 0.1 mM to 0.102 min^{-1} at 100 mM, representing a 30-fold increase (Table 3). This indicates that high IS significantly promotes physical straining and pore throat trapping of PS-MPs by compressing the double electric layer and shielding electrostatic repulsion. The desorption rates k_{det1} and k_{det2} at both sites approached zero under all conditions ($k_{det1} \approx 10^{-6}$ to 10^{-7} min^{-1}, $k_{det2} \approx 0$), confirming that the retention of PS-MPs in the presence of HA is essentially irreversible. Neither physical trapping nor chemical adsorption facilitates desorption.

3.4. Effect of iron oxyhydroxides coatings of quartz sand on transport and retention of PS-MPs

The BTCs and RPs of PS-MPs in the presence of HA under different λ conditions are shown in the Fig. 8. The transportability of PS-MPs in the saturated porous media decreased as the λ increased. For example, as λ increased, the time required for PS-MPs to exit the column increased, and the C/C_0 decreases. When λ is 0 (There is no iron oxyhydroxides coated quartz sand inside the column), the C/C_0 reached 0.796, while when λ reaches 0.75, the C/C_0 decreased to 0.391. An increased in the α values of PS-MPs were observed as the λ increased, especially at high λ (Table 2). Correspondingly, the mass recoveries of PS-MPs in the effluent decreased from 84.51 to 40.99% (Table 2), this trend aligns with observed behaviors in the transport of MPs within saturated sandy columns.[60] This may be attributed to the formation of nano- to micrometer scale iron oxide particle aggregates on the quartz sand surface by the hydroxy iron oxide coating, which significantly increases the micro-roughness and surface area of the medium.[80,81] The direct consequences of this coarse structure are: (1) at the pore scale, hydroxy iron oxide aggregates may partially block pore throats or create more tortuous flow paths, enhancing physical straining of PS-MPs; (2) at the particle scale, the rough surface increases contact points and friction coefficients between PS-MPs and the medium, making it harder for particles that come into contact to be resuspended by water flow. This explains why k_{att2} increase synchronously with increasing ω (Table 3), more hydroxy iron oxides mean more "physical barrier points," and these barrier points exhibit higher capture efficiency. Contrast to the untreated sandy column, the transport behaviors of PS-MPs were weakened in hydroxy iron oxide coated quartz sand, regardless of the presence of HA (Table 2). This might be due to the fact that the transport of PS-MPs in sand with iron oxyhydroxides was not sensitive to HA.[60] In addition, The ≡Fe–OH groups provided by the hydroxy iron oxide coatings serve as excellent chemical adsorption sites. In

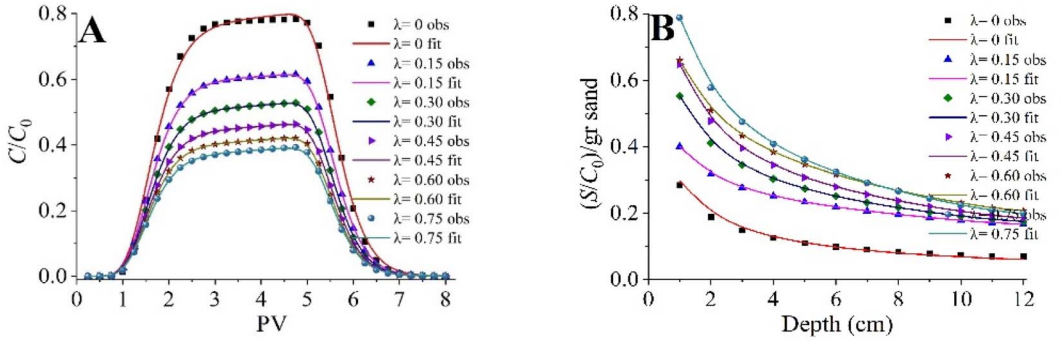

Fig. 8 Measured and fitted breakthrough curve (A) and retention profile (B) for PS-MPs under different λ at pH 6.0 in the presence of 10 mg L^{-1} HA.

the presence of HA, these sites may interact with PS-MPs through multiple pathways: Firstly, cations (Na^+) in the solution form bridges between negatively charged PS-MPs and negatively charged ≡Fe–O^-, causing the PS-MPs to become immobilized within the column.[82] Secondly, certain areas of the iron oxide coating may provide hydrophobic sites.[37] More importantly, the iron oxyhydroxides coated quartz sand surface exhibits a strong positive charge (12.79 mV) at pH 6.0 (Table 1), and the isoelectric point (pH_{PZC}) of iron oxyhydroxide is 8.4.[38] This may lead to PS-MPs strongly and irreversibly adsorb to the surface of the iron oxyhydroxides coated quartz sand through electrostatic adsorption. And the more quartz sands were coated with iron oxyhydroxides, the more PS-MPs (or PS-MPs-HA) will be adsorbed on its surface. In other words, the attachment is directly proportional to λ. Similarly, the time required for PS-MPs to occupy the most favorable attachment sites also increases with the increase of λ. Only after the sites related to iron oxyhydroxides are occupied can substantial penetration begin, which is consistent with the results found in previous related studies.[38] The strength of these chemical interactions far exceeds that of pure DLVO electrostatic forces, leading to a significant increase in k_{att1} and rendering adsorption irreversible once it occurs. For instance, compared with the experimental group where only HA concentration was varied, the total mass balance of PS-MPs gradually deteriorated with the increase of λ (102.33 to 93.49%). When λ is relatively large, the RPs cannot fully reflect the quality of PS-MPs in the sand. This might be because the PS-MPs retained on the iron oxyhydroxide coated quartz sand were not completely removed during the extraction process.

However, the retention of PS-MPs increased with the increases of λ, and the hyper-exponential shape of the RPs (Fig. 8B) is also more obvious. When λ increased from 0 to 0.75, the retention rates of PS-MPs increased about three times (from 17.82 to 52.49%), and these results indicate that RPs provide useful information on the quantitative aspects of PS-MPs.

3.5. Effect of pH on transport and retention of PS-MPs

The regulatory effect of pH on PS-MPs transport and retention behavior under specific conditions of HA concentration (10 mg L^{-1}), IS (0.1 mM), and hydroxy iron oxide coating content ($\omega = 0.15$) is shown in the Fig. 9. As shown in the figure, the transport and retention behaviors of PS-MPs were significantly affected by the solution pH presence of HA and IS. When the solution pH increases from 6.0 to 10.0, the BTCs shifts to the left, indicating faster transport rates of PS-MPs in the sandy column. At the same time, the C/C_0 of BTCs increases as the solution pH increases, indicating that the weakly alkaline solution is favorable for the transport of PS-MPs in porous media in this study.

The significant regulatory effect of pH on PS-MPs retention can be thoroughly explained from the perspectives of DLVO theory and surface chemistry. The isoelectric point of PS-MPs typically falls between pH 2.0 and 4.0.[37,82] Within the pH range of this study (6.0–10.0), the MPs surface carries a strong negative charge.[37,82] The iron oxyhydroxide coatings exhibits a higher isoelectric point (approximately pH 7–9).[83] At pH 6.0, it carries a positive or weakly negative charge. At pH 8.0–10.0, it becomes negatively charged due to deprotonation of the ≡Fe–OH group (≡Fe–OH → ≡Fe–O^- + H^+). Therefore, as the pH increases from 6.0 to 10.0, the electrostatic interactions between PS-MPs and the surface of the medium undergo a fundamental shift. At pH 6.0, electrostatic attraction or weak repulsion exists between PS-MPs (negatively charged) and iron oxyhydroxide coatings (positively or weakly negatively charged), resulting in a low DLVO energy barrier. Particles readily approach the surface and become retained. At pH 8.0–10.0, strong electrostatic repulsion exists between PS-MPs (strongly negatively charged) and iron oxyhydroxide coatings (negatively charged), significantly increasing the DLVO energy barrier. Particles struggle to overcome this barrier and approach the surface.[84] This increase in electrostatic repulsion directly leads to a significant decrease in k_{att1} – chemical adsorption requires particles to overcome an energy barrier to contact active sites on the surface, and an elevated barrier reduces the adsorption rate. In addition, the hydrodynamic sizes of PS-MPs shrink with increasing pH.[64] Both the deposition and size exclusion straining are weakened during the transport of PS-MPs under this condition, and it is reasonable for MPs to transport easily through saturated porous media.

Increased pH also affects the charge state and conformation of HA. HA contains numerous carboxyl and phenolic hydroxyl

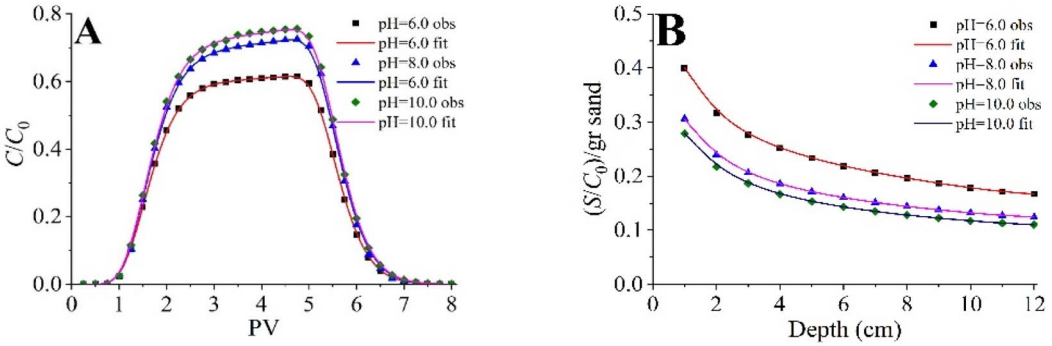

Fig. 9 Measured and fitted breakthrough curve (A) and retention profile (B) for PS-MPs under different pH condition at $\lambda = 0.15$ in the presence of 10 mg L^{-1} HA.

groups with pK_a values around 3–5 (primarily involving the dissociation of carboxyl groups),[85,86] which are fully deprotonated within the pH range of this study, carrying a strong negative charge. As pH rises, electrostatic repulsion within HA molecules intensifies, causing the molecular conformation to shift from coiled to extended. At pH 6.0, HA molecules adopt a relatively curled conformation, potentially partially masking the PS-MPs surface. At pH 8.0–10.0, HA molecules extend, forming a thicker steric hindrance layer that further enhances isolation between PS-MPs and the medium surface. This likely explains the significant decrease in S_{max1} – the steric hindrance layer formed by the extended HA conformation "shields" many available retention sites.

It is worth noting that when the pH value of the solution changes from 6.0 to 10.0, the value of k_{att2} decreases from 0.00545 to 0.00261 min^{-1}, with a change range of 52.11%. This disparity reveals the primary pathway through which pH affects physical retention not by reducing the efficiency of physical capture, but by diminishing the number of available sites for physical capture.[87] The steric barrier layer formed by the extended HA conformation may cover physical capture sites on the originally rough surface (such as pore throats and shadow zones), rendering these sites "inactive."[88] Simultaneously, enhanced electrostatic repulsion makes it difficult for PS-MPs to enter certain narrow pores, further reducing opportunities for effective physical capture.

Consistent with the trend in model parameters, the RPs exhibits a weakening hyper-exponential decay characteristic as pH increases (Fig. 9B). At pH 6.0, the RPs displays a typical hyper-exponential decay pattern: a high retention ratio at the inlet end with rapid decay. As pH rises to 8.0 and 10.0, the entire retention curve shifts significantly downward, the retention ratio at the inlet end decreases substantially, and the curve shape becomes flatter.

This morphological evolution can be perfectly explained by the model parameters: at pH 6.0, S_{max1}/C_0 reaches 1.42 g^{-1}, indicating a large number of chemical adsorption sites can efficiently capture PS-MPs; k_{att1} is 0.0545 min^{-1}, suggesting a significant contribution from chemical adsorption along the flow path. The combined effect of both factors produces a hyper-exponential curve characterized by high retention at the inlet and sustained capture along the flow path. When pH increased to 8.0 and 10.0, S_{max1}/C_0 sharply decreased to 0.50 and 0.41 g^{-1}, indicating a significant reduction in the number of chemical adsorption sites. Concurrently, k_{att2} decreased to 0.0333 and 0.0261 min^{-1}, diminishing the contribution of physical retention and a steep decline in capture efficiency at the inlet. Consequently, the entire retention curve shifted markedly downward, and the hyper-exponential characteristics weakened.

4. Conclusion

This study addresses the identified research gap by demonstrating that: (i) PS-MPs retention in saturated porous media involves two mechanistically distinct processes – chemical adsorption and physical retention, that respond differently to environmental factors; (ii) the TKSAD model, even with S_2 exhibiting negligible desorption, is necessary to capture these distinct mechanisms and their differential environmental responses; and (iii) the model parameters provide quantitative mechanistic insights that cannot be obtained from one kinetic site models or from breakthrough curves alone. These findings advance beyond previous studies that treated MPs retention as a single process or employed one kinetic site models that cannot distinguish between physical and chemical mechanisms.

5. Environmental implications

These findings have important implications for predicting the fate of MPs in natural aquatic and soil environments. In freshwater systems with low IS and circumneutral pH, the presence of NOM may facilitate MPs transport over long distances. In contrast, in seawater – intruded coastal aquifers or saline – alkali soils characterized by high IS, MPs are likely to be retained near the source zone, particularly in the presence of metal oxide minerals. The strong pH dependence suggests that acid rain events or alkaline pollution incidents could dramatically alter MPs mobility. Furthermore, the irreversible nature of retention ($k_{det} \approx 0$) implies that once deposited, MPs may persist in the subsurface even under changing geochemical

conditions, posing long-term ecological risks. Future studies should consider the coupled effects of multiple environmental factors and extend these findings to more complex natural porous media.

Author contributions

Abliz Abdurahman and Xiaoli Ma are the two co-first authors of this paper. Abliz Abdurahman: investigation, methodology, software, data curation, formal analysis, writing – original draft. Rui Gao: visualization, investigation, data curation. Xiaoli Ma: conceptualization, methodology, writing – review & editing. All authors have given approval to the final version of the manuscript.

Conflicts of interest

The authors declare no competing financial interest.

Data availability

The data supporting the findings of this study are included within the article and its supplementary information (SI) files hosted by the Royal Society of Chemistry. Supplementary information: experimental methods, additional supporting figures, tables, raw data summaries, and statistical analyses that further support the main findings of this study. See DOI: https://doi.org/10.1039/d5ra08025h.

Acknowledgements

This study was supported by the Research Fund for High-Level Talent of Xinjiang Medical University.

References

1 Y. Seo, V. Chevali, Y. Lai, Z. Zhou, G. Chen, P. Burey, S. Wang and P. Song, *Environ. Manage.*, 2025, **377**, 124556–124567.
2 I. M. Jaikumar, M. Tomson, A. Meyyazhagan, B. Balamuralikrishnan, R. Baskaran, M. Pappuswamy, H. Kamyab, E. Khalili and M. Farajnezhad, *Green Anal. Chem.*, 2025, **12**, 100202.
3 C. Geng, Y. Gao, H. Zhang, D. Xue, S. He, B. Wang, X. Wang and J. Zhao, *Environ. Chem. Lett.*, 2024, **22**, 691–713.
4 W. Li, G. Brunetti, A. Bolshakova and C. Stumpp, *Sci. Total Environ.*, 2024, **935**, 11.
5 Z. Jia, W. Wei, Y. Wang, Y. Chang, R. Lei and Y. Che, *Rev. Environ. Contam. Toxicol.*, 2022, **260**, 1–18.
6 H. Wang, J. Zhang, Y. Chen, Y. Xia, P. Jian and H. Liang, *Front. Mar. Sci.*, 2024, **11**, 1346275.
7 T. Mutshekwa, F. Mulaudzi, V. P. Maiyana, L. Mofu, L. F. Munyai and F. M. Murungweni, *PLoS One*, 2025, **20**, 313840–313854.
8 Y. Ankit, K. Ajay, S. Nischal, S. Kaushal, V. Kataria, E. Dietze and A. Anoop, *Environ. Pollut.*, 2024, **361**, 124629.
9 Y. Dahal and S. Babel, *Air Qual. Atmos. Health*, 2025, **18**, 425–445.
10 M.-P. Albert and J. Joaquim, *Toxics*, 2020, **8**, 40.
11 T. Wang, D. Liu, R. Liu, F. Yuan, Y. Ding, J. Tao, Y. Wang, W. Yu, Y. Fang and B. Li, *Environ. Sci. Technol.*, 2025, **59**, 7667–7677.
12 S. Kühn, J. A. v. Franeker, A. M. O'Donoghue, A. Swiers, M. Starkenburg, B. v. Werven, E. Foekema, E. Hermsen, M. Egelkraut-Holtus and H. Lindeboom, *Environ. Pollut.*, 2019, **257**, 113569.
13 S. Paul, S. Nath, S. Bhattacharjee and S. Mukherjee, *Blue Biotechnol.*, 2024, **1**, 1–8.
14 L. G. A. Barboza, L. R. Vieira, V. Branco, C. Carvalho and L. Guilhermino, *Sci. Rep.*, 2018, **8**, 15655.
15 Y. Zhang, D. Li, K. Hui, H. Wang, Y. Yuan, F. Fang, Y. Jiang, B. Xi and W. Tan, *J. Environ. Chem. Eng.*, 2025, **13**, 115806.
16 A. Huvet, L. Frère, C. Lacroix, E. Rinnert, C. Lambert and I. Paul-Pont, *Reg. Stud. Mar. Sci.*, 2025, **89**, 104279.
17 S. Emami, S. Bagheri and A. Gholamhosseini, *Environ. Sci. Pollut. Res.*, 2025, **32**, 26641–26651.
18 S. Oberbeckmann and M. Labrenz, *Ann. Rev. Mar. Sci*, 2020, **12**, 209–232.
19 N. Zhu, Z. Li, Y. Yu, Z. Liu, X. Liang, W. Wang and J. Zhao, *Ecotoxicol. Environ. Saf.*, 2025, **295**, 118138.
20 Y. Wang, L. Xu, H. Chen and M. Zhang, *Sci. Total Environ.*, 2022, **808**, 152154.
21 L. Zeng, C. Yuan, T. Xiang, X. Guan, L. Dai, D. Xu, D. Yang, L. Li and C. Tian, *Nanomaterials*, 2024, **14**, 1060.
22 Y. Wei, Y. Chen, X. Cao, T.-C. J. Yeh, J. Zhang, Z. Zhan, Y. Cui and H. Li, *Environ. Sci. Technol.*, 2024, **58**, 12.
23 F. Li, D. Huang, G. Wang, M. Cheng, H. Chen, W. Zhou, R. Xiao, R. Li, L. Du and W. Xu, *Sci. Total Environ.*, 2024, **926**, 171658.
24 M. Li, L. He, X. Zhang, H. Rong and M. Tong, *Environ. Pollut.*, 2020, **267**, 115534.
25 G. Hul, H. Okutan, P. L. Coustumer, S. R. Gentile, S. Zimmermann, P. Ramaciotti, P. Perdaems and S. Stoll, *Nanomaterials*, 2024, **16**, 529.
26 Y. Jiang, S. Zhou, J. Fei, Z. Qin, X. Yin, H. Sun and Y. Sun, *Water Res.*, 2022, **215**, 118262.
27 M. N. Singer, B. Mohsen, V. E. Katzourakis, M. R. A. Shehhi and C. V. Chrysikopoulos, *J. Environ. Chem. Eng.*, 2025, **13**, 118002.
28 X. Zhang, L. Wu, X. Han, Y. Shi, J. Huang, B. Ding, Y. Zhang, Z. Zhang, Y. Shi and F. Li, *Chemosphere*, 2025, **370**, 143942–143951.
29 D. Zhou, Y. Cai and Z. Yang, *Environ. Pollut.*, 2022, **293**, 118503.
30 M. Tan, L. Feng, S. Bian, J. Duan, X. Li, X. Sun, Y. Sun, S. Wang and X. Yuan, *ACS ES&T Eng.*, 2024, **4**, 1230–1239.
31 X. Wang, Y. Diao, Y. Dan, F. Liu, H. Wang, W. Sang and Y. Zhang, *Chemosphere*, 2022, **309**, 136658.
32 X. Wang, Y. Dan, Y. Diao, F. Liu, H. Wang, W. Sang and Y. Zhang, *Sci. Total Environ.*, 2022, **847**, 157576.
33 Y. Hao, F. Zhu, H. Cheng, S. Komarneni and J. Ma, *J. Phys. Chem. Solid.*, 2024, **185**, 111787.
34 S. Wang, R. Walker-Gibbons, B. Watkins, M. Flynn and M. Krishnan, *Nat. Nanotechnol.*, 2024, **19**, 485–493.

35 F. Feng, W. Ye, S. Xiang, X. Fan, X. Liu, H. Liu and W. Zhang, *Front. Environ. Sci. Eng.*, 2025, **19**, 142.
36 H. Luo, L. Chang, T. Ju and Y. Li, *ACS Omega*, 2024, **9**, 50064–50077.
37 M. Tan, L. Liu, M. Zhang, Y. Liu and C. Li, *J. Hazard Mater.*, 2021, **413**, 125410.
38 D. Wang, S. A. Bradford, R. W. Harvey, B. Gao, L. Cang and D. Zhou, *Environ. Sci. Technol.*, 2012, **46**, 2738–2745.
39 R. S. Stahl and B. R. James, *Soil Sci. Soc. Am. J.*, 1991, **55**, 1291–1294.
40 D. Wang, S. A. Bradford, M. Paradelo, W. J. G. M. Peijnenburg and D. Zhou, *Soil Sci. Soc. Am. J.*, 2012, **76**, 375–388.
41 D. P. Jaisi, N. B. Saleh, R. E. Blake and M. Elimelech, *Environ. Sci. Technol.*, 2008, **42**, 8317.
42 Y. Wang, L. Xu, H. Chen and M. Zhang, *Environ. Sci. Technol.*, 2022, **808**, 152154.
43 Q. Ma, Y. Sun, S. Zhou, X. Yin and H. Sun, *Environ. Manag.*, 2025, **377**, 124696.
44 H. Xu, Y. Zhang, W. Zhang, Y. Tang, Y. Zhou, P. Tang and T. Zhang, *Phys. Fluids*, 2024, **36**, 053301.
45 X. Chu, T. Li, Z. Li, A. Yan and C. Shen, *Water*, 2019, **11**, 2474.
46 L. Zeng, C. Yuan, T. Xiang, X. Guan, L. Dai, D. Xu, D. Yang, L. Li and C. Tian, *Nanomaterials*, 2024, **4**, 1060.
47 M. N. Singer, B. Mohsen, V. E. Katzourakis, M. R. A. Shehhi and C. V. Chrysikopoulos, *J. Environ. Chem. Eng.*, 2025, **13**, 118002.
48 J. F. Schijven and J. Simunek, *J. Contam. Hydrol.*, 2002, **55**, 113–135.
49 S. A. Bradford, J. Simunek, M. Bettahar, M. T. V. Genuchten and S. R. Yates, *Environ. Sci. Technol.*, 2003, **37**, 2242.
50 P. Babakhani, J. Bridge, R.-A. Doong and T. Phenrat, *Adv. Colloid Interface Sci.*, 2017, **246**, 75–104.
51 F. J. Leij, S. A. Bradford and A. Sciortino, *J. Contam. Hydrol.*, 2016, **195**, 40–51.
52 N. H. Pham and D. V. Papavassiliou, *Comput. Part. Mech.*, 2017, **4**, 87–100.
53 Y. F. Adrian, U. Schneidewind, S. A. Bradford, J. Simunek, T. M. Fernandez-Steeger and R. Azzam, *Environ. Pollut.*, 2018, **236**, 195–207.
54 J. Šimůnek, M. Th, v. Genuchten and M. Šejna, *Vadose Zone J.*, 2016, **15**, 1–25.
55 D. W. Marquardt, *SIAM J. Appl. Math.*, 1963, **11**, 431.
56 K. K. Norrfors, V. Mićić, O. Borovinskaya, F. v. d. Kammer, T. Hofmann and G. Cornelis, *Environ. Sci. Nano*, 2021, **8**, 1801.
57 N. Tufenkji and M. Elimelech, *Environ. Sci. Technol.*, 2004, **38**, 529.
58 M. Wang, T. Lu, W. Chen, H. Zhang, W. Qi, Y. Song and Z. Qi, *Colloids Surf., A*, 2020, **607**, 125486.
59 Z. Zhang, C. Wang, L. You, H. Chen, J. Dong, Q. Chen, Z. Wei, L. Zhang, M. Zhang and Z. Liu, *J. Hazard Mater.*, 2025, **499**, 140260.
60 D. Zhou, Y. Cai and Z. Yang, *Sci. Total Environ.*, 2024, **946**, 174270–174278.
61 I. Ioannidis, E. Antoniou and I. Pashalidis, *J. Environ. Chem. Eng.*, 2025, **13**, 115064.
62 L. Cai, L. Hu, H. Shi, J. Ye, Y. Zhang and H. Kim, *Chemosphere*, 2018, **197**, 142–151.
63 S. Dong, W. Cai, J. Xia, L. Sheng, W. Wang and H. Liu, *Environ. Pollut.*, 2021, **268**, 115828.
64 S. Li, H. Liu, R. Gao, A. Abdurahman, J. Dai and F. Zeng, *Environ. Pollut.*, 2018, **237**, 126–132.
65 X. Lu, L. Wang, J. Li, W. Li, R. Yan, X. Duan and Y. Tang, *Water Res.*, 2025, **281**, 123661.
66 A. Elrahmani, R. I. Al-Raoush, J. A. Hannun, M. T. Albaba and T. D. Seers, *Sci. Total Environ.*, 2025, **974**, 179238.
67 J. Wang, Y. Gao, L. Ren, H. Zhao, T. Long, Y. Li, C. Tsakiroglou, O. Alfarisi and X. Wang, *Chem. Eng. J.*, 2025, **520**, 166099.
68 X. Y. Xu, Y. Ji, D. Hu and B. J. Li, *Adv. Mater. Res.*, 2013, **781–784**, 2344–2348.
69 W.-K. Ho and K. S.-Y. Leung, *Water Res.*, 2021, **201**, 117317.
70 L. Cai, L. L. Hu, H. H. Shi, J. W. Ye, Y. F. Zhang and H. J. Kim, *Chemosphere*, 2018, **197**, 142–151.
71 O. S. Alimi, J. F. Budarz, L. M. Hernandez and N. Tufenkji, *Environ. Sci. Technol.*, 2018, **52**, 1704–1724.
72 O. Olena and S. Serge, *Environ. Sci. Nano*, 2018, **5**, 792–799.
73 W. Zhao, Z. Su, T. Geng, Y. Zhao, Y. Tian and P. Zhao, *Chemosphere*, 2022, **309**, 136593.
74 X. Wu, X. Lyu, Z. Li, B. Gao, X. Zeng, J. Wu and Y. Sun, *Sci. Total Environ.*, 2020, **707**, 136065.
75 S. Dong, C. Zhuo, Z. Wangwei, D. Zhiyue, L. Chuanbin and J. HanXia, *J. Nanopart. Res.*, 2019, **21**, 233.
76 H. Zhang, J. Sun and L.-H. Guo, *NanoImpact*, 2016, **3–4**, 75–80.
77 C. Peng, C. Shen, S. Zheng, W. Yang, H. Hu, J. Liu and J. Shi, *Nanomaterials*, 2017, **7**, 326.
78 S. A. Mason, D. Garneau, R. Sutton, Y. Chu, K. Ehmann, J. Barnes, P. Fink, D. Papazissimos and D. L. Rogers, *Environ. Pollut.*, 2016, **218**, 1045–1054.
79 A. M. Mahon, B. O'Connell, M. G. Healy, O. Connor, R. Officer, R. Nash and L. Morrison, *Environ. Sci. Technol.*, 2017, **51**, 810–818.
80 T. Wang, W. Cao, Y. Wang, C. Qu, Y. Xu and H. Li, *Ecotoxicol. Environ. Saf.*, 2023, **262**, 115179.
81 G. Li, *J. Phys. Conf.*, 2025, **2941**, 012010.
82 B. Chang, B. He, G. Cao, Z. Zhou, X. Liu, Y. Yang, C. Xu, F. Hu, J. Lv and W. Du, *Sci. Total Environ.*, 2023, **884**, 163832.
83 M. Kosmulski, E. Maczka, E. Jartych and J. B. Rosenholm, *Adv. Colloid Interface Sci.*, 2003, **103**, 57–76.
84 J. N. Ryan, M. Elimelech, R. A. Ard, R. W. Harvey and P. R. Johnson, *Environ. Sci. Technol.*, 1999, **33**, 63–73.
85 G. R. Choppin and L. Kullberg, *J. Inorg. Nucl. Chem.*, 1978, **40**, 651–654.
86 M. Fukushima, S. Tanaka, H. Nakamura and S. Ito, *Talanta*, 1996, **43**, 383–390.
87 J.-H. Choi, S.-O. Kim, E. Linardy, E. C. Dreaden, V. P. Zhdanov, P. T. Hammond and N.-J. Cho, *J. Phys. Chem. B*, 2015, **119**, 10554.
88 H. Fakour, Y.-F. Pan and T.-F. Lin, *Water Air Soil Pollut.*, 2015, **226**, 14.